Non-Isothermal Melt Crystallization Kinetics for CaO–Al$_2$O$_3$–B$_2$O$_3$ F-Free Mould Fluxes

Qifeng SHU,[1,2]* Jeferson Leandro KLUG[2] and Qiangqi LI[1]

1) School of Metallurgical and Ecological Engineering, University of Science and Technology Beijing, Beijing, 100083 China.
2) Department of Metallurgical and Materials Engineering, Federal University of Ceará, Fortaleza, CEP 60440-554 Brazil.

Efforts have been made to develop fluorine-free mould fluxes for the continuous casting of steel process. In this work the crystallization behaviour of fluorine-free mould slags based on the CaO–Al$_2$O$_3$–B$_2$O$_3$ system was investigated by differential scanning calorimeter (DSC) and scanning electron microscopy equipped with energy dispersive spectroscopy(SEM-EDS). The crystallization kinetics for Ca$_3$Al$_2$O$_6$ primary crystals was analysed by combining modified Avrami analysis with Friedman isoconversional method. Avrami parameter n is close to 4 for samples with the ratios w(CaO)/w(Al$_2$O$_3$)=1 and w(CaO)/w(Al$_2$O$_3$)=1.2, indicating a crystallization mechanism of continuous bulk nucleation and 3D crystal growth. The Avrami parameter n for samples with w(CaO)/w(Al$_2$O$_3$)=0.9 is close to 3, indicating instantaneous bulk nucleation and 3D crystal growth. The crystallization rate constant is the highest and half crystallization time is the lowest for the samples with w(CaO)/w(Al$_2$O$_3$)=0.9, indicating the fastest crystallization. In the initial stage, effective activation energies were mainly determined by the undercooling values. In the final stage, kinetic barrier for crystallization could have some influence on crystallization; for the investigated mould fluxes crystallization in the final stage is retarded by increasing w(CaO)/w(Al$_2$O$_3$) ratio. Thus crystallization mechanisms were elucidated and effective activation energy of crystallization for the first crystal which precipitates from melt was determined.

KEY WORDS: mould fluxes; crystallization; kinetics; melts; fluorine-free.

1. Introduction

Mould fluxes are widely applied for the continuous casting of steel process to provide the following functions: 1) to protect steel from oxidation; 2) to provide thermal insulation to protect the steel surface from freezing; 3) to lubricate the strand; 4) to provide optimal horizontal heat transfer; 5) to absorb inclusions from the steel. Commercial mould fluxes contain calcium fluoride (CaF$_2$) produce harmful gases during continuous casting, such as HF,[1] which in turn can impair health of steelworks operators and to speed up corrosion of the continuous casting machine; moreover, they are soluble in water which brings problems to disposal of waste water.[2] Therefore, in recent years, a lot of attempts were made to eliminate fluoride in mould fluxes compositions. Many kinds of fluoride-free mould fluxes based on CaO–SiO$_2$ system were developed.[3–10] Na$_2$O can decrease viscosity and melting temperature of mould fluxes and it was considered to be one of the substitutes for CaF$_2$ in commercial mould fluxes.[3] Addition of TiO$_2$ in mould fluxes could lead to precipitation of CaTiO$_3$ and CaSiTiO$_5$, which was considered to have potential to substitute for cuspidine in traditional mould fluxes, regarding control of

the horizontal heat transfer.[4–6] As one of the most effective fluxing agents, B$_2$O$_3$ can decrease the melting temperature and viscosity of mould fluxes. CaO–SiO$_2$–B$_2$O$_3$ based F-free mould fluxes have been developed by different research groups and have been deemed as the most promising F-free ones.[3,7–10] One substantial problem for a CaO–SiO$_2$–B$_2$O$_3$ based F-free mould flux which still exists so far is that this kind of mould flux has weaker crystallization ability when comparing with traditional mould fluxes.[3,7,11]

In view of the fact that CaO–Al$_2$O$_3$ based slag has better crystallization abilities than CaO–SiO$_2$ basedslag, the present authors developed new kinds of F-free mould fluxes based on the CaO–Al$_2$O$_3$–B$_2$O$_3$ system.[12] The viscosity values for the CaO–Al$_2$O$_3$–B$_2$O$_3$ based mould fluxes were located in the scope of traditional CaO–SiO$_2$ based mould fluxes, whereas the melting temperatures for CaO–Al$_2$O$_3$–B$_2$O$_3$ based mould fluxes are very close to those of traditional CaO–SiO$_2$ based ones. However, CaO–Al$_2$O$_3$–B$_2$O$_3$ based mould fluxes still need further investigation for adjusting their crystallization behaviour.

According to our previous publication,[12] the relevant technological parameters for developing mould fluxes for industrial application were discussed for similar mould fluxes compositions: viscosity at 1 300°C, melting characteristics, and crystallization temperature got from DTA curve. In the present paper, further investigation was per-

formed regarding mould fluxes crystallization. Crystallization behaviour for CaO–Al$_2$O$_3$–B$_2$O$_3$ based F-free mould fluxes with the wCaO/wAl$_2$O$_3$=0.9, 1.0 and 1.2 ratios was investigated using differential scanning calorimeter (DSC), X-ray diffraction (XRD) and scanning electron microscopy equipped with energy dispersive spectroscopy(SEM-EDS). The crystallization kinetics was studied, crystallization mechanisms were elucidated, and effective activation energy of crystallization for the first crystal which precipitated from melt was determined.

2. Experimental

2.1. Preparation of Glassy Samples

Analytical grade Al$_2$O$_3$ (>99%), Na$_2$CO$_3$ (>99.9%), Li$_2$CO$_3$ (>99.9%), CaCO$_3$ (>99%) and H$_3$BO$_3$ (>99.95%) powders were employed as raw materials for sample preparation. Na$_2$CO$_3$, Li$_2$CO$_3$ and H$_3$BO$_3$ were selected as sources for Na$_2$O, Li$_2$O and B$_2$O$_3$. Raw materials were mixed and put into a platinum crucible. Afterwards, samples were premelted in a furnace with MoSi$_2$ rods as heating elements at 1 350°C for 2 hours in air. Then, the melts were quenched into water to obtain glassy samples. The chemical compositions (wt.%) of the investigated samples were obtained by Electron Probe Micro-Analyzer (EPMA) and are listed in **Table 1**.

2.2. DSC Measurements

The glassy cullets were pulverized and subjected to the DSC using argon as purge gas with a thermal analyser STA 449 F3 Jupiter from the manufacturer Netzsch-Gerätebau GmbH. The samples were heated to 1 350°C and then cooled to room temperature, using alfa-Al$_2$O$_3$ as reference material. Platinum crucible covered by a platinum lid was used to minimize the evaporation of boron oxide and alkali oxides. For each DSC run approximately 25 mg of powder sample was employed. Before measurements temperature calibration, sensitivity calibration, and balance calibration were performed.

2.3. SEM-EDS and XRD Analyses

To examine the morphology and chemical composition

Table 1. Chemical composition of the investigated samples obtained by EPMA.

		Composition (wt.%)				
	w(CaO)/w(Al$_2$O$_3$)	CaO	Al$_2$O$_3$	B$_2$O$_3$	Na$_2$O	Li$_2$O
Sample 1 nominal	0.9	36.0	40.0	8.0	8.0	8.0
Sample 1 analyzed	0.9	36.0	38.1	9.2	8.3	8.0
Sample 2 nominal	1.0	38.0	38.0	8.0	8.0	8.0
Sample 2 analyzed	1.0	36.9	35.4	8.8	7.5	8.0
Sample 3 nominal	1.1	40.0	36.0	8.0	8.0	8.0
Sample 3 analyzed	1.2	40.1	33.2	7.7	7.6	8.0

of crystallization products, glassy samples were melted at 1 350°C in a MoSi$_2$ furnace and then cooled with the rate 5°C/min down to particular temperatures. After heat treatment at these temperatures, crystallization products were determined by SEM-EDS. The SEM-EDS analysis was performed using a FEI-MLA250 apparatus equipped with a Bruker EDS with the working voltage of 25 kV.

3. Results and Discussion

3.1. DSC Analysis

Figure 1 shows DSC curves for different cooling rates for the investigated samples. It could be seen that there are two obvious exothermic peaks and one minor exothermic peak on each curve. Cooling rates higher than 20 K/min were adopted since a preliminary thermogravimetric study had shown that evaporation is intense for lower cooling rates.

The precipitation sequence of crystals in CaO–Al$_2$O$_3$–B$_2$O$_3$ based F-free mould fluxes was determined in a previous work for the same samples.[12] Heat treatments at various temperatures were adopted to determine the possible precipitations in a previous work. After heat treatment, the samples were quenched and subject to SEM and XRD investigation to determine the precipitated phases. It was shown that Ca$_3$Al$_2$O$_6$ crystals are the first crystals which precipitate during cooling, followed by LiAlO$_2$ and Ca$_3$B$_2$O$_6$ ones. In order to verify the previous results the heat treatment described at section 2.3 were performed and then SEM micrographs were obtained, see **Fig. 2**. The micrographs of Fig. 2 are related to a thermal treatment which was performed at particular temperature for hours. This thermal treatment was intentionally performed to obtain 100% crystals (from glassy cullets as explained before), to identify all the possible phases. It was verified that all samples precipitated Ca$_3$Al$_2$O$_6$, LiAlO$_2$ and Ca$_3$B$_2$O$_6$ crystals. The darkest phase, the dark grey phase, and the light grey phase are LiAlO$_2$, Ca$_3$Al$_2$O$_6$, and Ca$_3$B$_2$O$_6$ crystals, respectively.

CCT diagrams for the investigated samples were built considering crystallization temperatures got from the DSC experiments, see **Fig. 3**. The crystallization temperature is defined here as the onset temperature of the first exothermic peak which is measured during cooling. It can be seen that the crystallization temperatures move towards lower temperatures when increasing the cooling rate, which could be due to the fact that the nucleation and growth rate of crystals are functions of viscosity and undercooling. A higher thermodynamic driving force, *i.e.* higher undercooling, was required to initiate the nucleation as viscosity of melts increase faster at higher cooling rate.[13] Moreover, it can also be observed that the sample 3 has the highest crystallization temperatures for all the cooling rates, *i.e.*, they increase when increasing the wCaO/wAl$_2$O$_3$ ratio.

The characteristic temperatures for the investigated samples at 35 K/min can be seen at **Table 2**. Besides the crystallization temperature, the *liquidus* temperature was also determined; it was obtained by considering the peak temperature for the last endothermic peak when heating the samples during DSC experiments.[14] The undercooling for onset crystallization (ΔT) is defined as the difference between *liquidus* temperature (T_L) and crystallization temperature (T_C) as follows:
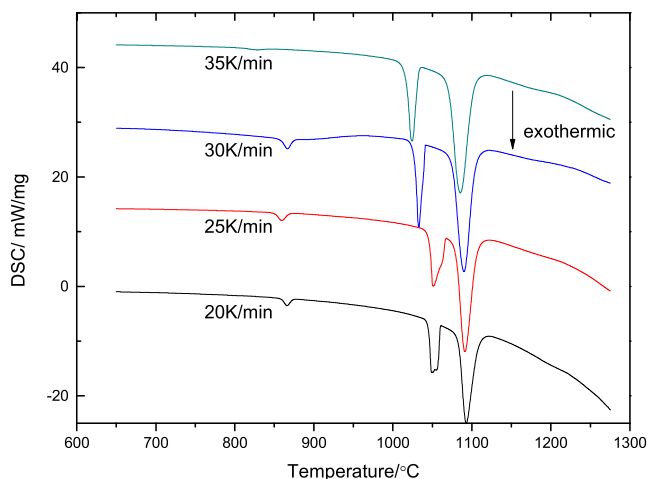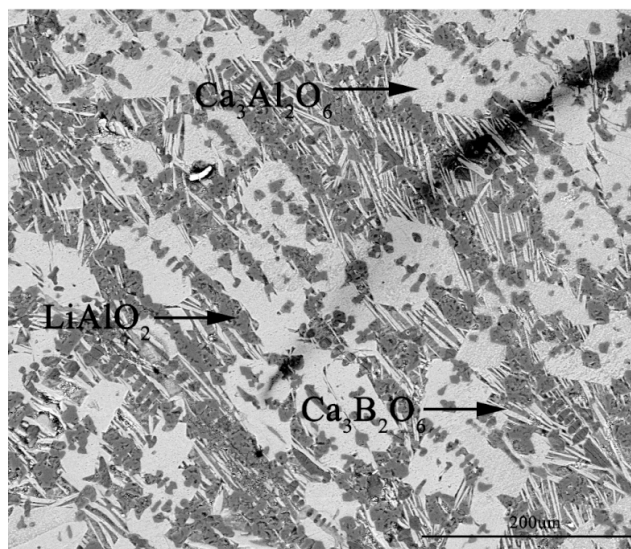
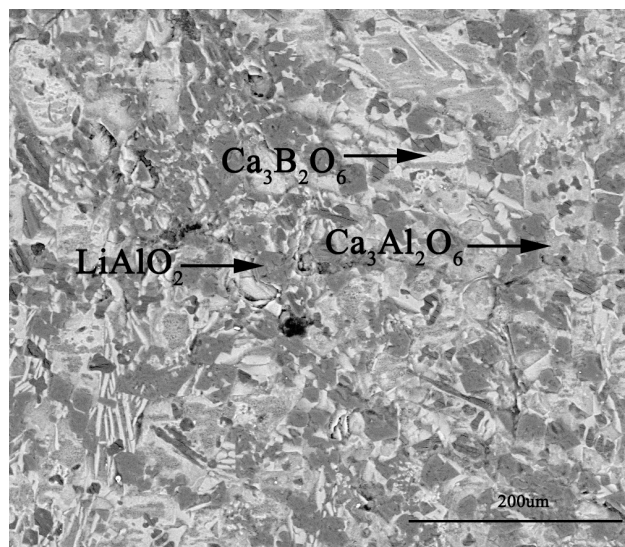(a) Sample 1
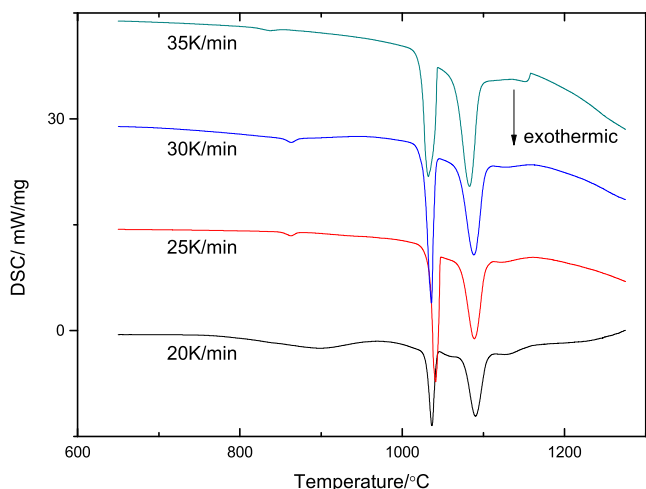
(b) Sample 2
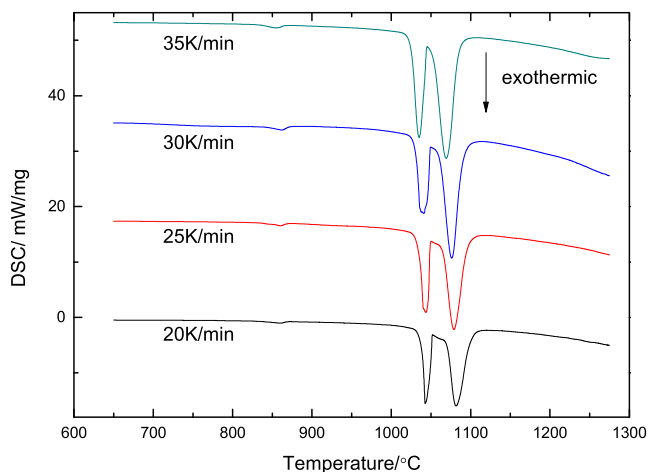
(c) Sample 3

Fig. 1. DSC curves at different cooling rates for the investigated samples. (Online version in color.)

(a) Sample 1

(b) Sample 2

(c)Sample 3

Fig. 2. SEM micrographs for the investigated samples, showing the crystalline phases which were identified.

$$\Delta T = T_L - T_C \quad \dots\dots\dots\dots\dots\dots\dots\dots (1)$$
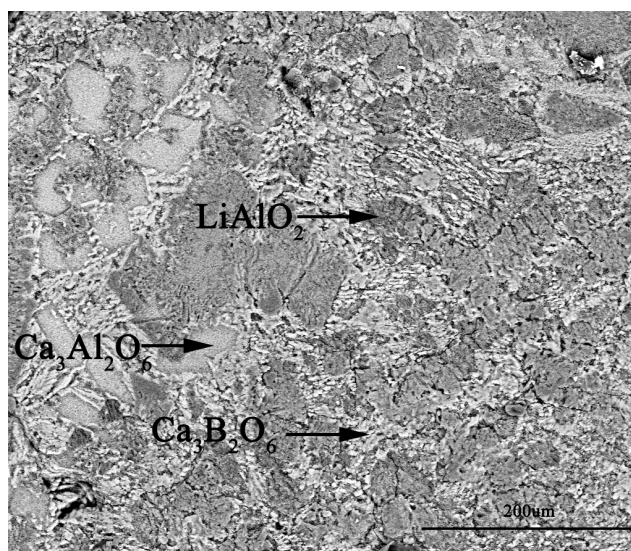
The crystallization kinetics of the primary crystallization – *i.e.* for $Ca_3Al_2O_6$– was analysed in the present work. The values of the relative crystallinity (α_T) can be obtained as a function of temperature (T) from DSC curves through the following equation:
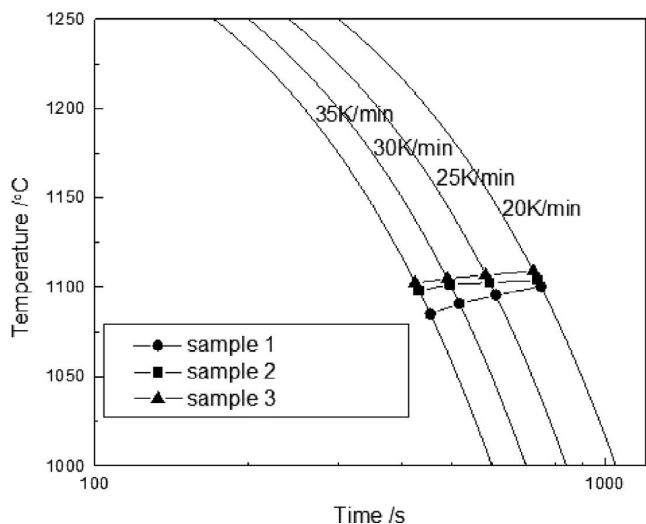
Fig. 3. CCT curves for the investigated samples, which were built using DSC experimental data.

Table 2. Characteristic temperatures and onset undercooling values at the cooling rate of 35 K/min for the investigated samples.

	Liquidus temperature T_L (°C)	Crystallization temperature T_c (°C) (at 35 K/min)	Undercooling $T_L - T_c$ (°C)
Sample 1	1 153	1 098	55
Sample 2	1 165	1 085	80
Sample 3	1 150	1 102	48

$$\alpha_T = \frac{\int_{T_0}^{T} (dH/dT)dT}{\int_{T_0}^{T_e} (dH/dT)dT} \quad \text{.......................} \quad (2)$$

where T, T_0 and T_e are the instantaneous, onset and end crystallization temperatures, respectively.

The heat flow rate determined by DSC is represented by dH/dT. Values of α_T at various cooling rates are shown at **Fig. 4**. The instantaneous temperature T can be converted to instantaneous time t through the following equation:

$$t = \frac{T_0 - T}{\beta} \quad \text{.................................} \quad (3)$$

Thus the relative crystallinity as a function of time (α_t) can be calculated as:

$$\alpha_t = \frac{\int_{t_0}^{t} (dH/dt)dt}{\int_{t_0}^{t_e} (dH/dT)dt} \quad \text{.........................} \quad (4)$$

where t_0 and t_e are the starting time and the ending time respectively.
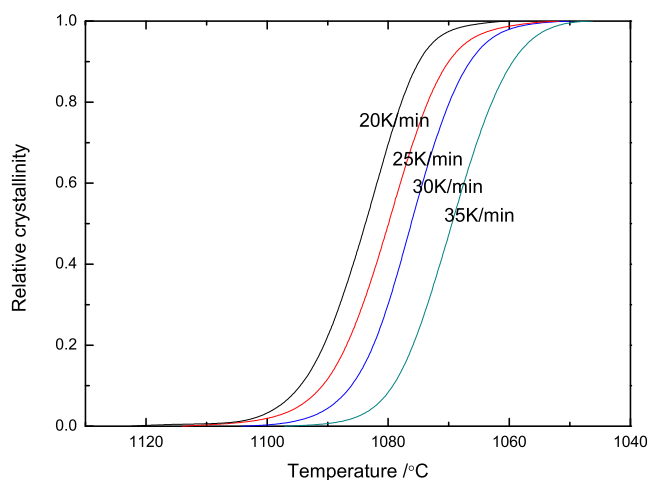
3.2. Modified Avrami Analysis

Crystallization kinetics is generally described by Avrami equation[15] in double logarithm form as follows:
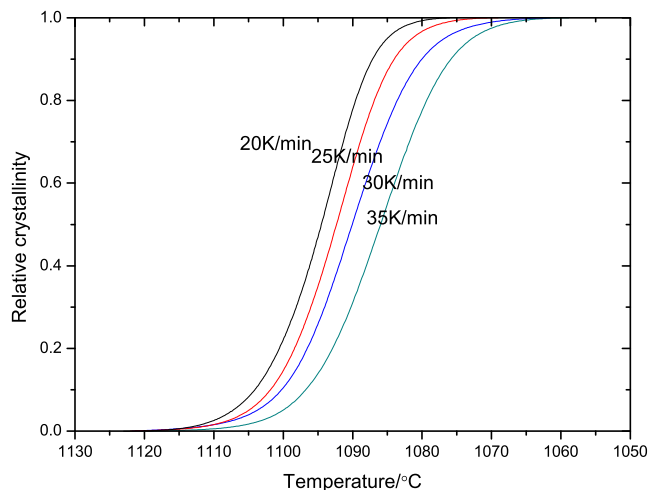
$$\ln(-\ln(1-\alpha)) = \ln Z_t + n\ln t \quad \text{...................} \quad (5)$$
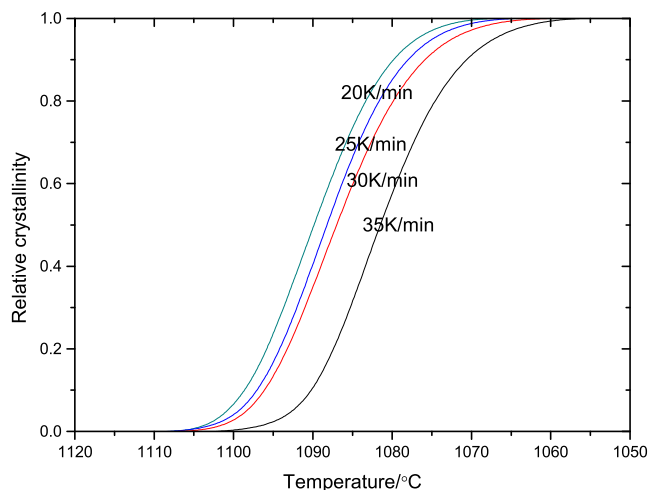
(a) Sample 1

(b) Sample 2

(c) Sample 3

Fig. 4. Relative crystallinity of $Ca_3Al_2O_6$ as a function of temperature for the investigated cooling rates. (Online version in color.)

Where α is the relative crystallinity, t is the crystallization time, Z_t is the crystallization rate constant, and n is a parameter indicating crystallization mechanism. In **Table 3** values of n corresponding to different nucleation and growth mechanisms can be seen.

Avrami equation cannot be directly used for non-

Table 3. Values of n for different nucleation and growth mechanisms.[21]

	Crystallization Mode	
	Diffusion controlled	Interfacial reaction controlled
Constant nucleation rate		
Three dimensional growth	2.5	4
Two dimensional growth	2	3
One dimensional growth	1.5	2
Instantaneous nucleation		
Three dimensional growth	1.5	3
Two dimensional growth	1	2
One dimensional growth	0.5	1
Surface nucleation	0.5	1

Table 4. Modified Avrami analysis results for various samples.

Sample	Sample no. (cooling rate)	n	Z_t	Z_c	$t_{1/2}$
Sample1	20 K/min	2.615	1.022	1.001	0.869
	25 K/min	2.847	1.418	1.014	0.875
	30 K/min	2.699	2.277	1.028	0.864
	35 K/min	2.939	3.248	1.034	0.873
Sample2	20 K/min	4.850	0.033	0.843	0.960
	25 K/min	3.890	0.237	0.944	0.924
	30 K/min	3.465	1.098	1.003	0.899
	35 K/min	3.650	1.994	1.020	0.900
Sample3	20 K/min	3.961	0.350	0.949	0.924
	25 K/min	4.010	0.488	0.972	0.919
	30 K/min	3.790	0.644	0.985	0.911
	35 K/min	4.058	1.241	1.006	0.912

isothermal crystallization. For these conditions, Jeziorny[16] proposed the modified Avrami analysis by using the following equation:

$$\ln\left(-\ln\left(1-\alpha\right)\right) = \beta \ln Z_c + n \ln t \quad \text{................ (6)}$$

where β is the cooling rate.

The new form of the crystallization rate constant parameter Zc can be obtained from Zt:

$$\ln Z_c = \ln Z_t / \beta \quad \text{.............................. (7)}$$

Zc is a dimensionless parameter which can be used for characterizing the kinetics of non-isothermal crystallization, and which is directly based on the theory formulated by Ziabicky.[17,18] This arises from the fact that values of this parameter are not dependent on the cooling rate; thus, Zc values should be the same for each material.

Half crystallization time $t_{1/2}$ could be calculated using Zc and n as follows:

$$t_{1/2} = \left(\frac{\ln 2}{Z_c}\right)^{1/n} \quad \text{.............................. (8)}$$

The calculated Z_t, Z_c, n and $t_{1/2}$ values for the analysed samples are listed in **Table 4**. It could be seen that sample 1 has the highest crystallization rate constants Z_c and lowest half crystallization time $t_{1/2}$. The n parameters for sample 2 and sample 3 are around 4; according to Table 3 this indicates that the constant nucleation rate with three-dimensional growth is the main mechanism of crystallization. It has been shown in Fig. 2 that $Ca_3Al_2O_6$ crystals have morphology of irregular blocks which is in consistence with 3D growth indicated by n parameters. Therefore, the morphology of $Ca_3Al_2O_6$ shown in Fig. 2 verifies the results of kinetic analysis. The values of n parameters for sample 1 is close to 3. This indicates that the crystallization mechanism of sample 1 is different. As shown in Fig. 2, $Ca_3Al_2O_6$ is still in morphology of irregular block for sample 1. From Table 3, the crystallization of sample 1 should proceed through instantaneous nucleation and three-dimensional growth. It was found that the $Ca_3Al_2O_6$ crystals in sample 1 are coarser than those in sample 2 and 3. The size of final crystals depends on not only nucleation but growth of crystals. The coaser $Ca_3Al_2O_6$ crystals in sample 1 compared with other samples indicate the faster nucleation and growth, which may be due to enhanced diffusion as discussed in Section 3.3. It was also shown by larger Zc parameter in sample 1 that the overall crystallization rate of sample 1 is also larger than other samples due to the enhanced nucleation and also growth.

3.3. Effective Activation Energy for Crystallization of $Ca_3Al_2O_6$ in CaO–Al_2O_3–B_2O_3 Based Mould Fluxes

Various models have been proposed to determine the activation energy for non-isothermal crystallization. Matusita equation was found to be only applicable to kinetic analysis for crystallization of glass during heating. It was clarified by Vyazovkin[19,20] that Kissinger method would provide invalid results for kinetic analysis of melt crystallization during cooling. In the present work the differential isoconversional method proposed by Friedman[21] was employed to obtain the effective activation energy for crystallization of $Ca_3Al_2O_6$. The effective activation energy of crystallization can be obtained at a given crystallization fraction through the following equation:

$$\ln\left(\frac{d\alpha}{dt}\right)_\alpha = -\frac{E_\alpha}{RT_\alpha} + C \quad \text{...................... (9)}$$

where $(d\alpha/dt)_\alpha$ is the instantaneous crystallization rate at the relative crystallinity α, T_α is the temperature at the relative crystallinity α, C is a constant, and E_α is the effective activation energy for crystallization. Plotting $\ln(d\alpha/dt)$ against T_α should give a straight line with slope $-E_\alpha/R$. Thus, effective activation energy for crystallization can be determined.

The dependences of effective activation energy for crystallization for various samples are shown in **Fig. 5**. It can be seen that the effective activation energies with respect to relative crystallinity from 0.1 to 0.8 for all samples are negative, indicating that crystallization of $Ca_3Al_2O_6$ become slower with increasing temperature. That is to say, the crystallization of $Ca_3Al_2O_6$ during cooling follows anti-Arrhenius behaviour, which was found in crystallization of
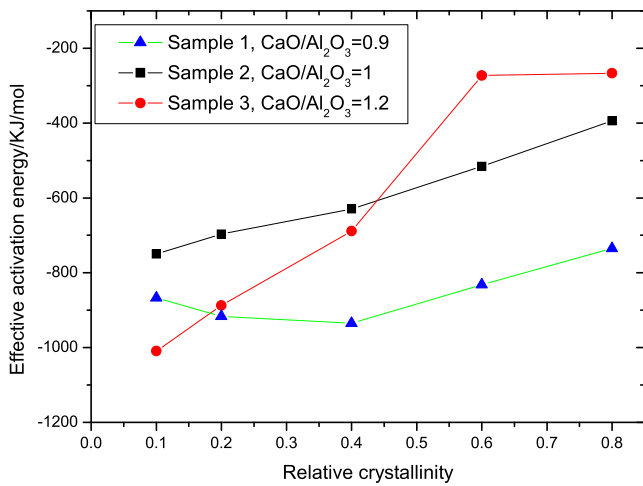
Fig. 5. Effective activation energy for crystallization of $Ca_3Al_2O_6$ as a function of relative crystallinity for the investigated samples. (Online version in color.)

polymer and traditional mould fluxes. The anti-Arrhenius behaviour was discussed by Vyazovkin et al.[19,20] and Cho[22,23] et al. The increase of crystallization rate with decreasing temperature should be due to the increase of thermodynamic driving force for nucleation.

According to the Classical Nucleation Theory, the nucleation rate is related to the Gibbs free energy of crystallization as follows[24]

$$I = I_0 \exp\left(-\frac{\Delta G_D + W}{RT}\right) \dots\dots\dots (10)$$

$$W = \frac{16\pi}{3}\frac{\sigma^3}{\Delta G_V^2} \dots\dots\dots (11)$$

Where I is the nucleation rate, I_0 is the pre-exponential factor, ΔG_D is the kinetic barrier for nucleation, W is the thermodynamic barrier term for nucleation, σ is crystal-melt surface energy per unit area of crystal, and ΔG_V is the thermodynamic driving force for nucleation per unit volume of crystals which is related to undercooling (T_L-T) through the following equation:

$$\Delta G_v = \Delta H_v\left(\frac{T_L - T}{T_L}\right) \dots\dots\dots (12)$$

where ΔH_v is the melting enthalpy per unit volume of crystals.

Crystallization from melts usually takes place at much higher temperature than crystallization from glasses, and therefore the undercooling values for crystallization from melts are much lower than that for crystallization from glasses. With the decrease of temperature, the undercooling and thermodynamic driving force are increased, and thereby the nucleation and crystallization rates of melts increased. Thus, an anti-Arrhenius behavior for crystallization from melts could be observed.

It could be also seen from Fig. 5 that the effective activation energy for crystallization of $Ca_3Al_2O_6$ for sample 2 and sample 3 increases with increasing of relative crystallinity. Effective activation energy for crystallization of $Ca_3Al_2O_6$ for sample 1 firstly shows a slight decrease and then an

increase with increasing of relative crystallinity. From Eqs. (10) to (12), the thermodynamic barrier W should decrease with decreasing of temperature. As relative crystallinity increases, the crystallization temperature decreases, and then effective activation energy (mainly determined by –W value) should increases.

According to Eqs. (10)–(12), the values of effective activation energy for samples with lower undercooling values should be more negative. In the area of low relative crystallinity, the sample 2 with $w(CaO)/w(Al_2O_3)=1.0$ has the highest value of effective activation energy; it agrees with the fact that it has the highest value of undercooling. This indicates that crystallization of sample 2 is more difficult when comparing with the other ones in the early stage of crystallization.

For relative crystallinity higher than 0.6, Sample 1 has the lowest effective activation energy values and Sample 3 has the highest ones, which indicates that the crystallization was retarded by increasing $w(CaO)/w(Al_2O_3)$ ratio. This result is also in consistence with the modified Avrami analysis which showed that sample 1 has the highest crystallization rate constant and the lowest half crystallization time. It could be also observed that the effective activation energy for sample 3 increases rapidly with increasing of the relative crystallinity. Since the kinetic barrier for crystallization could have some influence on the late stage of crystallization, the rapid increase and the high value of effective activation energy for sample 3 with the highest $w(CaO)/w(Al_2O_3)$ ratio could indicate that the kinetic barrier for crystallization is higher than that of other samples. It is well known that Al_2O_3 has an amphoteric behavior in slags.[25] The role of Al_2O_3 in structure of slag could vary with slag compositions. In order to form aluminate network, AlO_4^{5-} anions need to be charge compensated by metal cations.[24] The crystallization of $Ca_3Al_2O_6$ would lead to a continuous decrease of $w(CaO)/w(Al_2O_3)$ ratio during cooling. Therefore, in the final stage of crystallization, the $w(CaO)/w(Al_2O_3)$ ratio would decrease a lot, which could lead to insufficient charge compensation of AlO_4^{5-} anions. In this case, increasing $w(CaO)/w(Al_2O_3)$ ratio would lead to the fact that more AlO_4^{5-} anions are charge-compensated by Ca^{2+}, and thereby increasing the degree of polymerization of aluminate network. The diffusion of ions in slag would be retarded by more polymerized network. Therefore, the kinetic barrier for the slag with larger $w(CaO)/w(Al_2O_3)$ ratio is higher. For the investigated mould fluxes, the crystallization in the final stage is retarded by increasing $w(CaO)/w(Al_2O_3)$ ratio.

4. Conclusion

The non-isothermal crystallization kinetics of CaO–Al_2O_3–B_2O_3 based fluoride free mould fluxes was investigated in the present work. The following conclusions could be drawn:

(1) The crystalline phases precipitated from mould fluxes are $Ca_3Al_2O_6$, $Li_2Al_2O_4$ and $Ca_3B_2O_6$. Crystallization temperature of mould fluxes increases with increasing $w(CaO)/w(Al_2O_3)$ ratio. The undercooling for onset crystallization of sample 2 with $w(CaO)/w(Al_2O_3)=1.0$ is the lowest.

(2) Modified Avrami analysis on crystallization of

$Ca_3Al_2O_6$ showed that the Avrami parameter n is close to 4 for samples with $w(CaO)/w(Al_2O_3)=1$ and 1.1, indicating a crystallization mechanism of continuous bulk nucleation and 3D crystal growth. The Avrami parameter n for samples with $w(CaO)/w(Al_2O_3)=0.9$ is close to 3, indicating instantaneous bulk nucleation and 3D crystal growth. The crystallization rate constant Z_c is the highest and half crystallization time $t_{1/2}$ is the lowest for sample with $w(CaO)/w(Al_2O_3)=0.9$, indicating the fastest crystallization.

(3) The effective activation energies of crystallization of $Ca_3Al_2O_6$ for all samples are negative, showing anti-Arrhenius behaviour. The crystallizations of all samples are mainly controlled by thermodynamic driving force for nucleation. In the initial stage, effective activation energies were mainly determined by the undercooling values. The sample 2 with $w(CaO)/w(Al_2O_3)=1$ has the largest undercooling value and therefore has the largest effective activation energy value. In the final stage, kinetic barrier for crystallization could have some influence on the crystallization. Sample 3 with $w(CaO)/w(Al_2O_3)=1.2$ has the largest effective activation energy value due to retarded diffusion. The crystallizations of the investigated mould fluxes in the final stage are retarded by increasing $w(CaO)/w(Al_2O_3)$ ratio.

Acknowledgements

REFERENCES

1) K. C. Mills, A. B. Fox, Z. Li and R. P. Thackray: *Ironmaking Steelmaking*, **32** (2005), 26.
2) A. I. Zaitsev, A. V. Leites, A. Litvina and B. M. Mogutnov: *Steel Res.*, **65** (1994), 368.
3) A. B. Fox, K. C. Mills, D. Lever, C. Bezerra, C. Valadares, I. Unamuno, J. J. Laraudogoitia and J. Gisby: *ISIJ Int.*, **45** (2005), 1051.
4) H. Nakada and K. Nagata: *ISIJ Int.*, **46** (2006), 441.
5) G. H. Wen, S. Sridhar, P. Tang, X. Qi and Y. Q. Liu: *ISIJ Int.*, **47** (2007), 1117.
6) Z. Wang, Q. Shu and K. Chou: *ISIJ Int.*, **55** (2015), 709.
7) Q. Shu, Z. Wang, J. L. Klug, K. Chou and P. R. Scheller: *Steel Res. Int.*, **84** (2013), 1138.
8) L. Zhou, W. Wang and K. Zhou: *ISIJ Int.*, **55** (2015), 1916.
9) J. Yang, J. Zhang, Y. Sasaki, O. Ostrovski, C. Zhang, D. Cai and Y. Kashiwaya: *ISIJ Int.*, **56** (2016), 574.
10) J. L. Klug, M. M. S. M. Pereira, E. L. Nohara, S. L. Freitas, G. T. Ferreira and D. Jung: *Ironmaking Steelmaking*, **43** (2016), 559.
11) J. Yang, J. Zhang, Y. Sasaki, O. Ostrovski, C. Zhang, D. Cai and Y. Kashiwaya: *Metall. Mater. Trans. B*, **48** (2017), 2077.
12) J. Li, B. Kong, B. Galdino, J. Xu, K. Chou, Q. Liu and Q. Shu: *Steel Res. Int.*, **88** (2017), 1600485.
13) M. D. Seo, C. B. Shi, J. W. Cho and S. H. Kim: *Metall. Mater. Trans. B*, **45** (2014), 1874.
14) Q. Shu, Z. Wang and K. Chou: *High Temp. Mater. Process.*, **32** (2013), 281.
15) M. Avrami: *J. Chem. Phys.*, **7** (1939), 1103.
16) A. Jeziorny: *Polymer*, **19** (1978), 1142.
17) A. Ziabicki: *Appl. Polym. Symp.*, **6** (1967), 1.
18) A. Ziabicki: *Faserforsch. Textiltech.*, **18** (1967), 142.
19) S. Vyazovkin: *Macromol. Rapid Commun.*, **23** (2002), 771.
20) S. Vyazovkin and N. Sbirrazzuol: *J. Phys. Chem.*, **107** (2003), 882.
21) H. L. Friedman: *J. Polym. Sci. C*, **6** (1964), 183.
22) M. D. Seo, C. B. Shi, H. Wang, J. W. Cho and S. H. Kim: *J. Non-Cryst. Solids*, **412** (2015), 58.
23) M. D. Seo, C. B. Shi, J. Y. Baek, J. W. Cho and S. H. Kim: *Metall. Mater. Trans. B*, **46** (2015), 2374.
24) V. M. Fokin, E. D. Zanotto, N. S. Yuritsyn and J. W. Schmelzer: *J. Non-Cryst. Solids*, **352** (2006), 2681.
25) J. H. Park, D. J. Min and H. S. Song: *Metall. Mater. Trans. B*, **35** (2004), 269.
26) M. J. Toplis and D. B. Dingwell: *Geochim. Cosmochim. Acta*, **68** (2004), 5169.